INTERNATIONAL JOURNAL OF
Minerals, Metallurgy and Materials

Volume 31, Number 10, October 2024
Page 2173

Research Article https://doi.org/10.1007/s12613-023-2818-z

A simple route for preparation of TRIP-assisted Si–Mn steel with excellent performance using direct strip casting

Hui Xu[1,2], *Lejun Zhou*[1,2)✉], *Wanlin Wang*[1,2)], *and Yang Yi*[1,2)]

1) School of Metallurgy and Environment, Central South University, Changsha 410083, China
2) National Center for International Research of Clean Metallurgy, Central South University, Changsha 410083, China
(Received: 5 October 2023; revised: 21 December 2023; accepted: 26 December 2023)

Abstract: The complex producing procedures and high energy-consuming limit the large-scale production and application of advanced high-strength steels (AHSSs). In this study, the direct strip casting (DSC) technology with unique sub-rapid solidification characteristics and cost advantages was applied to the production of low-alloy Si–Mn steel with the help of quenching & partitioning (Q&P) concept to address these issues. Compared this method with the conventional compact strip production (CSP) process, the initial microstructure formed under different solidification conditions and the influence of heat treatment processes on the final mechanical properties were investigated. The results show that the initial structure of the DSC sample is a dual-phase structure composed of fine lath martensite and bainite, while the initial structure of the CSP sample consists of pearlite and ferrite. The volume fraction and carbon content of retained austenite (RA) in DSC samples are usually higher than those in CSP samples after the same Q&P treatment. DSC samples typically demonstrate better comprehensive mechanical properties than the CSP sample. The DSC sample partitioned at 300°C for 300 s (DSC-Pt300) achieves the best comprehensive mechanical properties, with yield strength (YS) of 1282 MPa, ultimate tensile strength (UTS) of 1501 MPa, total elongation (TE) of 21.5%, and product of strength and elongation (PSE) as high as 32.3 GPa·%. These results indicate that the excellent mechanical properties in low-alloy Si–Mn steel can be obtained through a simple process (DSC−Q&P), which also demonstrates the superiority of DSC technology in manufacturing AHSSs.

Keywords: direct strip casting; sub-rapid solidification; quenching and partitioning; TRIP-assisted AHSSs; microstructure

1. Introduction

Advanced high strength steels (AHSSs) have attracted great attention from both academia and industry, due to their excellent comprehensive mechanical properties, especially the lightweight and energy-saving effects in automobile applications. Transformation-induced plasticity (TRIP) assisted bainitic ferrite steels [1–2], medium-Mn steels [3–5], and quenching & partitioning (Q&P) steels [6–7] are of the 3rd generation AHSSs. However, the applications of them are not extensive mainly due to the complex casting & rolling and heat treatment processes, as well as the high production costs. These steels are mostly of the cold-rolled and annealed products, and processed through a complex route involving conventional continuous casting (CCC) or compact strip production (CSP)–multiple hot-rolling/cold rolling–reheating to austenitizing temperature for heat treatment [8–10]. Moreover, simultaneously improving the strength and elongation is also a big challenge for AHSSs, unless a large number of alloying elements are added to obtain abundant austenite at room temperature.

Previous studies have proven that CCC and CSP (with long process, complex steps, and high costs) cannot achieve this target. Thus, the direct strip casting (DSC) technology, which is a model of green short-process near-final shape manufacturing technology in the steel industry with rapid development in recent years [11–12], has been expected to solve these problems. DSC technology can directly produce steel strips with a thickness of 1–5 mm from liquid metal, eliminating the expensive and energy-consuming multiple rolling and finishing steps [13–15]. Moreover, DSC is performed without mold flux, which means that the molten steel is directly contacted with the mold, resulting in higher heat flow and solidification rates. Many fundamental studies on DSC technology focused on dual phase (DP) steels [16–17], silicon steels [18–19], high/medium-Mn steels [20–22], and stainless steels [23–24]. Daamend *et al.* [21] produced a Fe–29Mn–0.3C twinning induced plasticity (TWIP) steel using the DSC technology and found micro-segregation in the as-cast strip. After additional cold-rolling and annealing, the uniformity of sample structure and grain size was significantly improved. Xiong *et al.* [16–17] used the sub-rapid solidification DSC process to prepare the DP and TRIP strips, and then studied the influence of hot-rolling and heat treatment parameters on their microstructure and properties. The results indicate that the dislocation strengthening and grain

✉ Corresponding author: Lejun Zhou E-mail: l.j.zhou@hotmail.com

boundary strengthening effects occurred in these thin strips after hot-rolling, so the yield strength of them was improved.

Although these previous researches suggest that the sub-rapid solidification characteristics have favorable effects on tailoring the microstructure, the microstructure of as-cast strip obtained under sub-rapid solidification condition is usually full fine martensite (high strength but insufficient plasticity), which is a problem restricting the improvement of the plasticity. In order to break through the restriction of strength on elongation and obtain AHSS with excellent comprehensive mechanical properties, it is essential to increase the proportion of soft phase in the microstructure while retaining the ultra-fine martensite lath in the as-cast structure to ensure high strength. Liu *et al.*'s research [25] has shown that the optimal mechanical properties of TRIP-assisted steels are achieved through the ideal balance between the volume fraction and stability of retained austenite (RA).

Therefore, the co-existence of austenite and ferrite in the microstructure is of great significance for the improvement of plasticity. To meet this expectation on mechanical properties and cost of final products, in this study, the DSC technology with unique sub-rapid solidification characteristics and cost advantages was applied to the production of low-alloy Si–Mn steel with the help of Q&P concept. Compared this method with the conventional CSP process, the initial microstructure formed under different solidification conditions and the influence of heat treatment processes on the final mechanical properties were investigated. Hopefully, the results obtained here can provide some idea to the production of low-carbon Si–Mn AHSS in industry.

2. Experimental

2.1. Material and experimental processes

The chemical composition of the target steel is Fe–0.21C–2.03Mn–2.1Si (wt%), which is similar to the composition of general commercial TRIP steel. Mn was added to avoid the austenite to ferrite transformation at high temperatures. Si was used to suppress carbide precipitation during the quenching, tempering, and partitioning steps. The DSC samples were obtained through the sub-rapid thermal simulation device "dip-tester" developed by the Iron and Steel Research Center of Central South University, China, while the CSP samples for the comparative study came from a CSP production line of a steel enterprise. Fig. 1(a) shows the schematic diagram of the dip-tester thermal simulator, and Fig. 1(b) shows the specific simulation experimental process and the size information of the as-cast sample. The dip-tester is mainly composed of heating and temperature control system, atmosphere control system, and sub-rapid cooling system. The heating and temperature control system consists of an intermediate frequency induction furnace, an infrared thermometer on the top of the crucible, and a proportion integration differentiation (PID) controller. The atmosphere control system consists of a vacuum pump, inlet and outlet gas pipes, and two oxygen partial pressure measuring instruments installed in the inlet and outlet gas pipes respectively, which can simulate the atmosphere environment of molten metal in the industrial field (N_2 protection in this experiment). The sub-rapid cooling system consists of a pair of strong water-cooled copper dies set in parallel and a mechanical system connected to them. During the experiment, a pair of parallel water-cooled copper molds were immersed in the liquid steel and pulled out in time. The molten steel contacted with two water-cooled copper molds at the same time and began to solidify and grew, so as to simulate the industrial twin-roll strip caster. The insertion speed of the copper mold could be controlled and adjusted by the mechanical system to simulate the rotation speed of the crystallization roll of the twin-roll strip caster. The residence time of the copper mold in the liquid steel could also be adjusted by the sub-rapid cooling system to simulate the solidification time of the liquid steel on the crystallization roll in actual production. Our previous research [26–27] demonstrated that the device can accurately simulate different environments by adjusting different experimental variables, and finally obtain the casting strip structure very similar to the industrial site, which has reliable simulation.

Then, the DSC and CSP samples were subjected to a same hot-rolling and heat treatment. The phase transition temperature was measured by the thermal expansion experiment, and the A_{c1} (the temperature at which austenite starts to form), A_{c3} (the temperature at which ferrite starts transforming into austenite), M_s (the temperature at which martensite transformation begins), M_f (the temperature at which martensite transformation is completed), and B_s (the temperature at which bainite starts to form) are 754, 870, 376, 250, and 591°C, respectively. The annealing treatment was carried out in the full austenite region at 950°C to obtain optimal composite microstructure ratio of martensite and austenite, followed by quenching and partitioning process. To further verify the feasibility of the design and explore the role of partitioning time in this process, two different partitioning times of 300 and 900 s were designed as variables (hereinafter referred to as DSC-Pt300, DSC-Pt900, CSP-Pt300, and CSP-Pt900). The specific routes are shown in Fig. 2.

2.2. Microstructure characterization

The detailed microstructural observation was characterized by means of optical microscope (OM, DM4M), field emission scanning electron microscopy (FE-SEM, JSM-7900F), and X-ray diffraction (XRD, D/max 2550VB, Cu K_α radiation, 40 KV, and 150 mA). The samples for OM and FE-SEM were manually polished step by step with sandpaper of different roughness, mechanically polished with diamond, and etched by 4vol% nitric acid alcohol. The volume fraction of RA was determined by XRD through direct comparison method [28] of the integrated intensities of the $(200)_\alpha$, $(211)_\alpha$, $(200)_\gamma$, $(220)_\gamma$, and $(311)_\gamma$ peaks in the 2θ degree ranging from 35° to 105° with a scanning rate of 5°/min. The calculation formula is as follows:

$$V_\gamma = I_\gamma C_\alpha / (I_\gamma C_\alpha + I_\alpha C_\gamma) \quad (1)$$

where V_γ is the volume fraction of RA, I_α is the integral intensity of the martensite peak, C_α is the correlation coeffi-

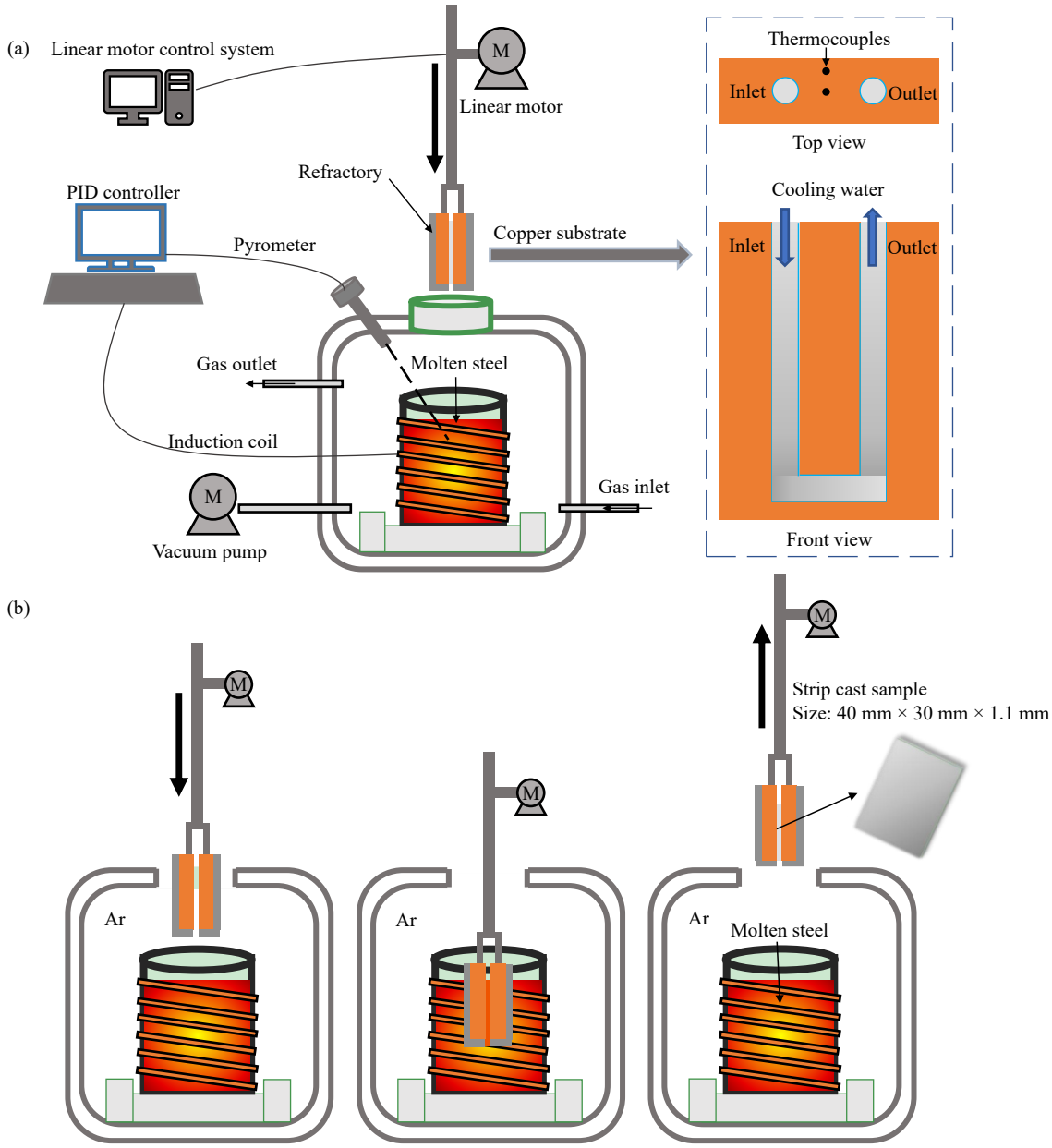

Fig. 1. Schematic diagrams of (a) dip-tester thermal simulator and (b) corresponding experimental process.

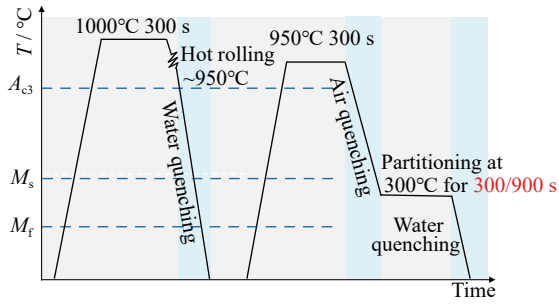

Fig. 2. Hot-rolling and Q&P heat treatment process. *T*—Temperature.

cient of martensite, I_γ is the integral intensity of the austenite peak, and C_γ is the correlation coefficient of RA.

The carbon content of RA (χ_C) was estimated using the following equation [28–29]:

$$a_\gamma = 3.556 + 0.0453\chi_C + 0.00095\chi_{Mn} + 0.0056\chi_{Al} \quad (2)$$

where a_γ is the lattice constants of the austenite measured by XRD, Å; χ_C, χ_{Mn}, and χ_{Al} are the contents of carbon, manganese, and aluminum, respectively.

2.3. Tensile tests

Uniaxial tension tests for the DSC and CSP samples under static deformation condition were performed using a universal material testing machine at room temperature, with a tensile rate of 1 mm/min. Prior to the tensile tests, the tensile samples were mechanical polished to remove the influence of possible oxide layers on both sides.

3. Results and discussion

3.1. Original microstructure and mechanical properties

Fig. 3(a)–(d) shows the initial OM and SEM microstructures of DSC and CSP as-cast samples. It can be observed

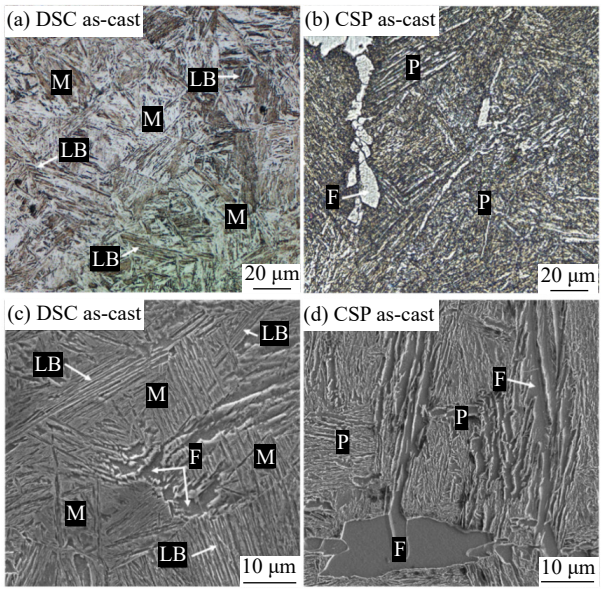

Fig. 3. Initial OM and SEM microstructures of DSC and CSP as-cast samples: (a) OM image of DSC as-cast sample; (b) OM image of CSP as-cast sample; (c) SEM image of DSC as-cast sample; (d) SEM image of CSP as-cast sample. M: Martensite; F: Ferrite; LB: Lower bainite; P: Pearlite.

that the initial microstructure of the two samples were completely different, which are greatly related to the different cooling conditions during solidification processes. The DSC sample is composed of abundant lath martensite and little lower bainite (LB), while the initial microstructure of CSP sample is pearlite/ferrite multiphase, in which ferrite is mainly multilaterally shaped. According to previous studies, the cooling rate of DSC process could as high as 10^3 K·s^{-1}, which is much higher than that of conventional CSP process [30]. Under the condition of sub-rapid solidification, once the molten steel comes into contact with the water-cooled copper mold, it rapidly cools down, equivalent to a quenching process, leading to the microstructural transformation [27], ultimately forming a composite microstructure composed of abundant fine lath martensite. The room-temperature tensile engineering stress–strain curves in Fig. 4(a) shows that the comprehensive mechanical property of DSC sample is much better than that of CSP sample. Table 1 lists the mechanical properties indexes of each curve. The ultimate tensile strength (UTS) and yield strength (YS) of as-cast DSC sample are as high as 1268 MPa and 874 MPa, respectively, with a total elongation (TE) of 13.1%, which is much higher than that of CSP sample. Fig. 4(b)–(e) shows the fracture morphologies of DSC and CSP as-cast samples. The fracture morphology of DSC sample is composed of abundant dense circulars/elliptical equiaxed dimples, with some large and deep dimples scattered throughout, showing the characteristics of ductile fracture. The fracture morphology of CSP sample is composed of numerous small and shallow dimples scattered around the river-pattern dissociation steps, showing a typical brittle fracture behavior. These results suggest that the DSC process is the most efficient and energy-saving compared with CSP technology.

In addition, the microstructure of as-cast sample formed under sub-rapid solidification is a composite structure of fine lath martensite and bainite, which exhibits excellent comprehensive mechanical properties compared to the pearlite and ferrite structure of CSP sample. In comparison, DSC samples have better comprehensive mechanical properties. According to previous studies [27,30], the heat flux is about 1–2 MW/m^2 for traditional continuous casting process and 2.5 MW/m^2 for CSP process, while the heat flux of DSC process can be as high as 6–8 MW/m^2. In conclusion, although the chemical composition of the test steels is identical, the processed samples have two completely different microstructures due to the huge difference in cooling conditions between CSP and DSC techniques. The structure determines

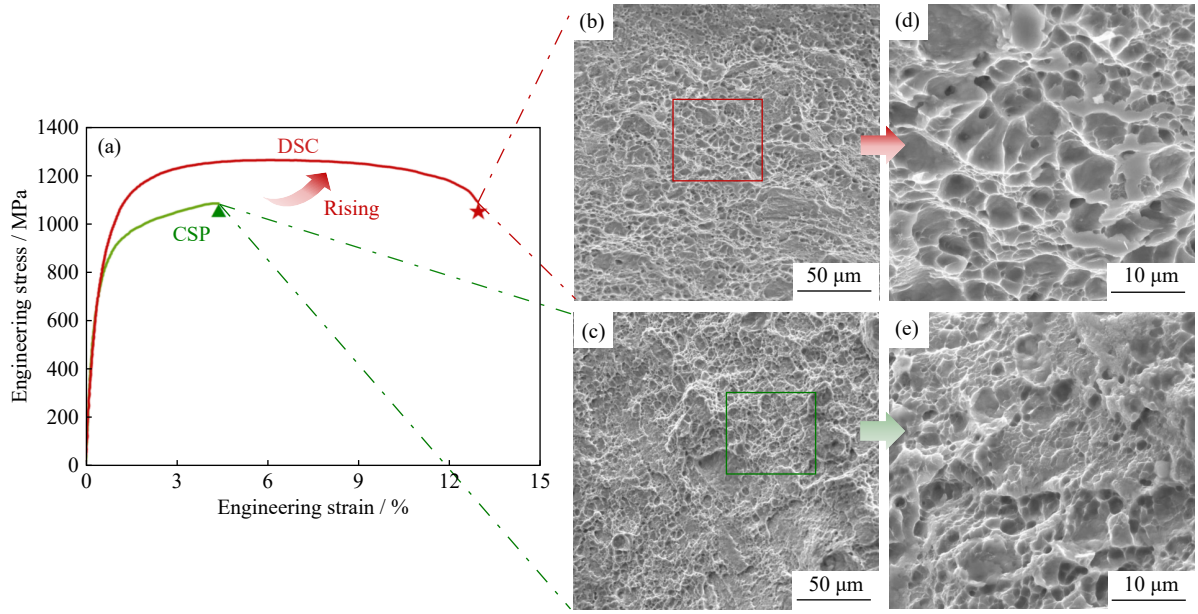

Fig. 4. (a) Engineering stress–strain curves of DSC and CSP as-cast samples; fracture morphologies of (b, d) DSC as-cast sample and (c, e) CSP as-cast sample.

Table 1. Mechanical properties of the as-cast samples

Sample	YS / MPa	UTS / MPa	TE / %	PSE / (GPa·%)
DSC as-cast	874	1268	13.1	16.6
CSP as-cast	754	1088	4.0	4.4
DSC-Pt300	1282	1501	21.5	32.3
DSC-Pt900	1031	1252	22.3	27.9
CSP-Pt300	636	1315	13.2	17.4
CSP-Pt900	594	1117	21.5	24.0

the properties, and the different microstructures make their mechanical properties also change greatly.

3.2. Microstructure and mechanical properties after Q&P treatment

Fig. 5(a)–(d) shows the SEM microstructures of DSC-Pt300, DSC-Pt900, CSP-Pt300, and CSP-Pt900 samples, respectively. It can be observed that the microstructures have undergone significant changes compared to as-cast samples. DSC samples transforms into a composite microstructure consisting of abundant refined lath martensite, RA, and a small amount of bainite. Different martensite lath blocks show different distribution orientations, while within the same martensite block, the width of the lath is very uniform with a parallel distribution. With the prolongation of partitioning time, it can be observed that a small amount of structure has not been eroded in the DSC-Pt900 sample, which is the formation of the "fresh" martensite (FM) during the secondary quenching process. The substructure and chemical composition of the primary quenched martensite and FM should be different because they are formed at different times, originating from the primary austenite with different carbon contents. After initial quenching, most of austenite transforms into martensite, while the untransformed metastable austenite continues the partitioning process. Due to differences in carbon content, morphology, size, and other factors, these metastable austenite grains exhibit varying degrees of stability, with less stable austenite grains easily

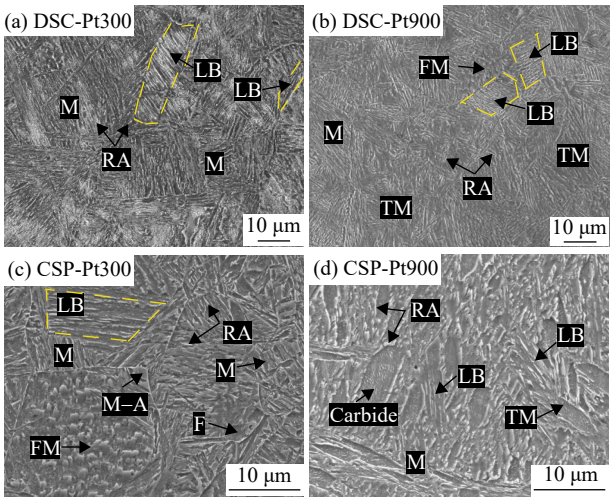

Fig. 5. SEM morphologies after Q&P treatment: (a) DSC-Pt300 sample; (b) DSC-Pt900 sample; (c) CSP-Pt300 sample; (d) CSP-Pt900 sample. M–A: Martensite–austenite island.

transforming into FM during the secondary quenching stage. Additionally, it can be observed that the convexity of some martensite laths in DSC-Pt900 sample decreases, indicating that the tempering process has occurred, forming tempered martensite (TM) structures.

The microstructure of the CSP-Pt300 sample consists of martensite, ferrite, bainite, RA, and a large amount of FM, indicating that some austenite transforms into martensite during the secondary quenching stage due to the insufficient stability. Due to the relatively short partitioning time, C does not reach a completely uniform distribution state in the austenite, and there is a concentration gradient in the same austenite grains. Therefore, this part of austenite is prone to transformation into FM during the secondary quenching stage. With the partitioning time increasing from 300 to 900 s, the lath martensite tends to be blurred with obvious carbide precipitation behavior for CSP-Pt900 sample, indicating that tempering process takes place.

Although the target steel contains a certain amount of non-carbide forming elements Si and Al, prolonged partitioning still leads to the formation of tempered martensite, which can only partially suppress the generation of carbide precipitation during the partitioning stage. After the initial quenching, there are stress fields around the dislocations and substructures of the carbon-rich martensite, where the energy of the gap positions near these defects are lower than that of the normal lattice gap positions. This leads to the redistribution of carbon at these low-energy sites. As a result, some C atoms segregate and precipitate between martensite laths in the form of carbides, with the partition time extending to 900 s.

Fig. 6 shows the XRD results of DSC and CSP samples before and after tensile tests. Four diffraction peaks, $(111)_\gamma$ $(200)_\gamma$, $(220)_\gamma$, and $(311)_\gamma$ which belong to austenite, are clearly observed. These characteristic peaks indicate the presence of RA in the microstructure after Q&P treatment. After fracture, the intensity of the austenite diffraction peak significantly decreases. These changes suggest that the most of RA undergoes martensitic transformation during the tensile process, and then enhances the strength and plasticity of the material through the TRIP effect. Additionally, it is noticeable that the intensity of austenite diffraction peaks in DSC-Pt300 is lower than that in DSC-Pt900, while the intensity of austenite diffraction peaks in CSP-Pt300 is higher than that in CSP-Pt900. This indicates that with prolonged partitioning time, samples with different initial structures exhibit distinct trends in austenite content.

Fig. 7 shows the columnar statistical graph of the calculated RA volume fraction and average carbon content in the RA before tensile tests. For DSC samples, the the volume fraction of RA shows an increasing trend and the carbon content shows a decreasing trend with prolonged partitioning time. The volume fraction of RA in DSC-Pt300 is 11.91vol%, with a maximum carbon content of 1.36wt%. The DSC-Pt900 sample has the highest RA volume fraction of 13.42vol%, with a carbon content of 1.28wt%. For CSP

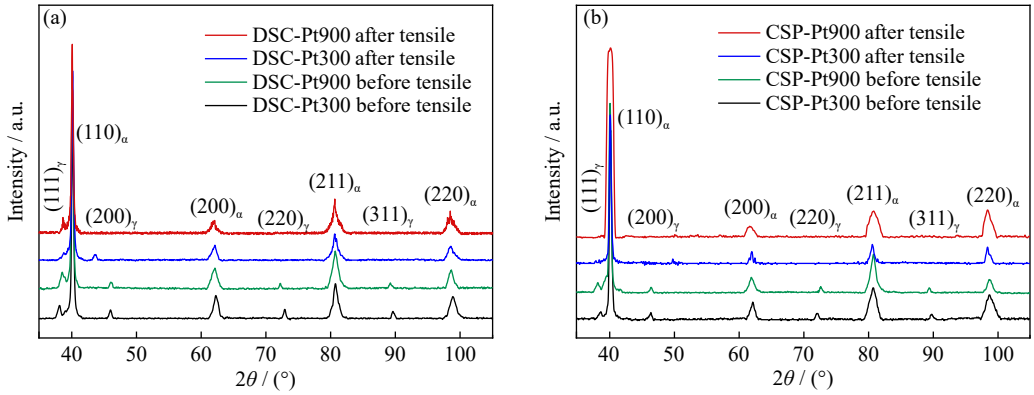

Fig. 6. XRD patterns before and after tensile test after Q&P treatment: (a) DSC samples; (b) CSP samples.

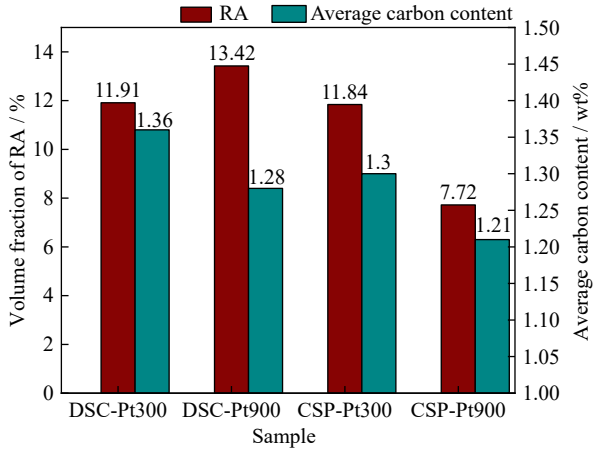

Fig. 7. Volume fraction and average carbon content of RA.

samples, as the partitioning time increases from 300 to 900 s, the volume fraction of RA decreases by 4.12vol%, with an average carbon content in RA decreases by 0.09wt%. Therefore, the changes in volume fraction and average carbon content of RA is inconsistent with the extension of partitioning time. The volume fraction of RA fluctuates greatly, while the difference in average carbon content among different samples of RA is not significant (1.21wt% to 1.36wt%). This indicates that the partitioning process does not make the carbon content in RA continuously increase, but make it fluctuate within a certain range. Once the extreme value is exceeded, the carbon will precipitate out in the form of cementite.

The above results suggsest that the volume fractions of RA in DSC samples and CSP samples do not change synchroneously with the extension of partitioning time after the same Q&P treatment due to the different initial microstructures. Generally, the volume fraction of RA in DSC samples is typically higher than that in CSP samples. For CSP-Pt900, C completes the homogenization process in RA. However, excessive partitioning time can lead to carbide precipitation, and then reduces the stability of RA. As a result, martensitic transformation occurs in the process of secondary quenching, leading to a decrease in the volume fraction of RA at room temperature. This indicates that an excessive long partitioning time can not increase the carbon content of RA, but leads to the tempering of martensite and the precipitation of cementite. At this time, the inhibition effect of Al/Si element on precipitation may not be significant, and the precipitation of cementite greatly reduces the carbon that can be distributed into austenite. Less carbon in austenite can reduce the stability of RA, and ultimately affecting the volume fraction of RA at room temperature. For DSC-Pt900, appropriately extending the partitioning time can promote the diffusion of carbon. Although carbon diffuses rapidly in martensite, it takes a long time for uniformly distributing in austenite.

3.3. Comparison of mechanical properties between DSC and CSP samples

The room-temperature tensile engineering stress–strain curves are shown in Fig. 8. The DSC samples generally have better comprehensive mechanical properties compared to the CSP samples after the same heat treatment. Table 1 lists the specific mechanical performance of each sample. The DSC-Pt300 sample exhibits the most excellent comprehensive mechanical properties, with YS of 1282 MPa, UTS of 1501 MPa, TE of 21.5%, and a high PSE of 32.3 GPa·%. Compared to the DSC-Pt300 sample, the UTS of DSC-Pt900 sample reduces about 250 MPa, while TE remains similar. The volume fraction of RA in the DSC-Pt900 sample (13.42vol%) is slightly higher than that in the DSC-Pt300 sample (11.91vol%), but its elongation is similar to that of the DSC-Pt300 sample due to the stability of RA. Despite having the highest volume fraction of RA, the average carbon

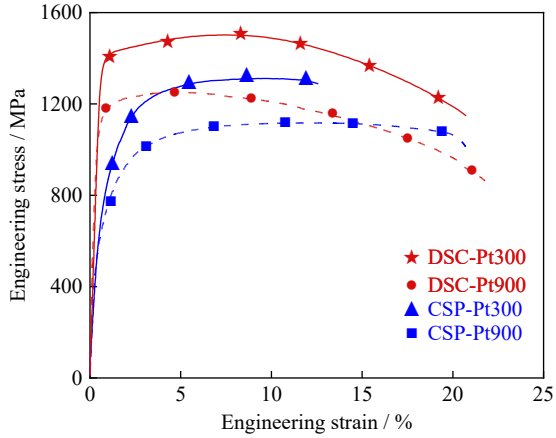

Fig. 8. Engineering stress–strain curves of samples after Q&P treatment.

content in RA of the DSC-Pt900 sample is lower, resulting in lower mechanical stability. Therefore, the additional part of RA has no significant effect on improving elongation, compared to DSC-Pt300 sample. In addition, the martensite in the DSC-Pt900 sample is tempered with the prolongation of the partitioning time (Fig. 5(b): martensite laths become less prominent), which results in a reduction of about 250 MPa in UTS compared to the DSC-Pt300 sample.

The TE of CSP samples significantly increases by approximately 9%–17.5%, compared to the as-cast sample. As the partitioning time is prolonged to 900 s, the strength of both DSC and CSP samples decreases significantly, while the TE increases to varying degrees. Compared with that of the CSP-Pt300 sample, the TE of the CSP-Pt900 sample increases about 7.3%, accompanied by a decrease of 198 MPa in UTS. Compared with DSC samples formed under sub-rapid solidification, the grain size of CSP samples is significantly coarser after the same heat treatment (Fig. 5). Therefore, the partitioning time of 300 s is relatively short for CSP-Pt300 sample. Although the average carbon content in RA is higher than that of CSP-Pt900 samples, it has not yet reached a completely uniform distribution state in austenite, as there is a concentration gradient in the same austenite grain. This part of austenite is easily transformed into FM during the secondary quenching stage (Fig. 5(c)) due to insufficient stability. However, FM has a more brittle performance due to its higher carbon content. With the prolongation of the partitioning time, the CSP-Pt900 sample has an obvious tempering phenomenon. Some C atoms segregate and precipitate between martensite laths in the form of carbide (Fig. 5(d)), resulting in a decrease in the content of C used to stabilize austenite. Although a longer partitioning time reduces the total austenite content, the austenite exhibits good stability (no FM was observed in Fig. 5(d)), resulting in better overall mechanical properties than the CSP-Pt300 sample. Therefore, it can be concluded that the strength and elongation of DSC and CSP decrease significantly and the elongation increases when the partitioning time increases from 300 to 900 s. When the partitioning time is 900 s, there is a certain degree of loss in the comprehensive mechanical properties of both group samples.

Fig. 9(a)–(d) exhibits the morphologies of fracture after the tensile tests. The macroscopic fracture morphologies of all samples are dark-colored and goose-plush like. The fracture surface along the thickness direction mainly consists of the central fiber region and the shear lip region. The central fiber region is the origin of fracture, with significant surface

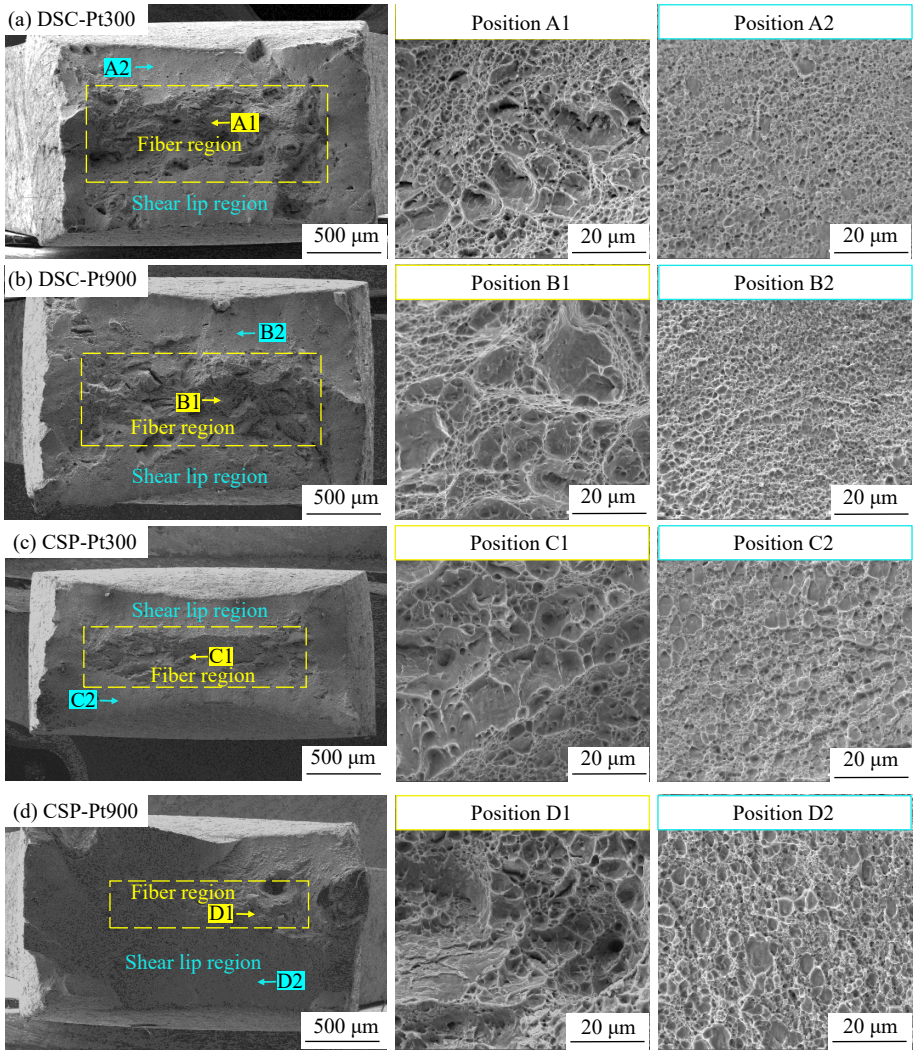

Fig. 9. Fracture morphologies of (a) DSC-Pt300 sample, (b) DSC-Pt900 sample, (c) CSP-Pt300 sample, and (d) CSP-Pt900 sample.

fluctuations and composed of many fiber "peaks" or "pits". The surface of the shear lip region, composed of many small and shallow circle dimples, is relatively smooth. This shear lip region is formed when the final crack occurs, showing typical brittle fracture characteristics. The morphology of fracture fiber region in DSC samples is similar. It is a typical micropore aggregation fracture characteristics, with many large and deep circular/elliptical dimples distributed between relatively small dimples. The fiber region of CSP samples is also composed of many dimples, but the size, depth, and number of dimples are relatively small. Note that there are river-like detachment steps in local regions, especially for the CSP-Pt900 sample, showing the characteristics of brittle cleavage fracture. Through comparative analysis, it can be found that the fracture types of the four group samples are all quasi-dissociation fracture (between brittle fracture and ductile fracture), with dimple fracture being the main type. Compared to CSP samples, the DSC samples exhibit a greater number and depth of dimples, with a more uniform distribution. To a certain extent, the morphology of dimples can reflect the plastic deformation degree of the sample under the action of external force. Generally, samples with larger and deeper dimples exhibit greater plastic deformation and better plasticity. The DSC-Pt300 sample has the highest TE, indicating the occurrence of maximum plastic deformation and the largest and deepest dimple sizes. The fracture morphology corresponds well to the elongation of the samples.

In summary, the initial microstructure of DSC sample is composed of a large amount of fine lath martensite, resulting in good mechanical properties in the as-cast samples. The ultimate goal of Q&P treatment is to obtain a composite structure with reasonable ratio of lath martensite and austenite. The carbon partitioning process during Q&P treatment allows the austenite to be retained at room temperature, increasing the proportion of soft phase in the matrix and laying a good microstructure foundation for its good plasticity. Therefore, the plasticity of DSC sample is obviously improved compared to the as-cast sample, and the overall comprehensive mechanical properties are optimized. The microstructure of CSP samples transforms from initial ferrite + pearlite to martensite, ferrite, and a small amount of RA. The formation of a large number of hard phase martensite provides a good microstructure basis for the high strength of steel, while the presence of soft phase ferrite and austenite further guarantees the plasticity of steel. Although the comprehensive mechanical properties of the CSP samples have also improved after undergoing the same Q&P treatment, the degree of enhancement is clearly not as significant as the DSC samples.

4. Conclusions

This work has achieved the goal of obtaining excellent mechanical properties in the low-alloy trip-assisted Si–Mn steel through a simple process, demonstrating the superiority of DSC technology in manufacturing AHSSs. The main conclusions are as follows.

(1) The structure of the as-cast sample formed by DSC process is a composite structure of lath martensite and bainite. Compared with the pearlite and ferrite structure of CSP as-cast sample, the DSC as-cast sample has higher comprehensive mechanical properties with YS of 874 MPa, UTS of 1268 MPa, and TE of 13.1%.

(2) After the same Q&P treatment, the martensite bundles of DSC samples are smaller in width and more compact in arrangement than those of CSP samples, indicating that the morphology of microstructure obtained after heat treatment depends not only on the parameters of heat treatment, but also on the initial microstructure.

(3) Compared to CSP samples, DSC samples typically exhibit superior comprehensive mechanical properties, due to the appropriate volume fraction and stability of RA. The DSC-Pt300 sample shows outstanding comprehensive mechanical performance with a PSE of up to 32.3 GPa·%, achieving the expected performance of low-alloy AHSS.

(4) Due to the differences in initial microstructure, the volume fraction and carbon content of RA in DSC and CSP samples do not change synchronously with the prolongation of partitioning time. The volume fraction of RA in DSC samples is usually higher than that in CSP samples. The results indicate that the carbon content in RA is a necessary condition for its stable existence at room temperature, but it is not always the dominant factor and cannot fully reflect the final volume fraction of RA.

Acknowledgements

This work was financially supported by the National Natural Science Foundation of China (No. 52130408), and the Natural Science Foundation of Hunan Province, China (No. 2022JJ10081).

Conflict of Interest

The authors have no relevant financial or non-financial interests to disclose.

References

[1] X.L. Gui, G.H. Gao, H.R. Guo, F.F. Zhao, Z.L. Tan, and B.Z. Bai, Effect of bainitic transformation during BQ&P process on the mechanical properties in an ultrahigh strength Mn–Si–Cr–C steel, *Mater. Sci. Eng. A*, 684(2017), p. 598.

[2] F. Peng, X.L. Gu, and Y.B. Xu, Tailoring austenite stability and mechanical behaviors of IQ&P steel via prior bainite formation, *Mater. Sci. Eng. A*, 822(2021), art. No. 141663.

[3] R. Ding, Z.B. Dai, M.X. Huang, Z.G. Yang, C. Zhang, and H. Chen, Effect of pre-existed austenite on austenite reversion and mechanical behavior of an Fe–0.2C–8Mn–2Al medium Mn steel, *Acta Mater.*, 147(2018), p. 59.

[4] Y.J. Wang, S. Zhao, R.B. Song, and B. Hu, Hot ductility behavior of a Fe–0.3C–9Mn–2Al medium Mn steel, *Int. J. Miner. Metall. Mater.*, 28(2021), No. 3, p. 422.

[5] Y. Ma, R. Zheng, Z.Y. Gao, *et al*., Multiphase-field simulation of austenite reversion in medium-Mn steels, *Int. J. Miner.*

Metall. Mater., 28(2021), No. 5, p. 847.
[6] S. Yan, X.H. Liu, W.J. Liu, H.F. Lan, and H.Y. Wu, Comparison on mechanical properties and microstructure of a C–Mn–Si steel treated by quenching and partitioning (Q&P) and quenching and tempering (Q&T) processes, *Mater. Sci. Eng. A*, 620(2015), p. 58.
[7] J.P. Lai, J.X. Yu, and J. Wang, Effect of quenching-partitioning treatment on the microstructure, mechanical and abrasive properties of high carbon steel, *Int. J. Miner. Metall. Mater.*, 28(2021), No. 4, p. 676.
[8] J. Zhou, Y.L. Kang, and X.P. Mao, Precipitation characteristic of high strength steels microalloyed with titanium produced by compact strip production, *J. Univ. Sci. Technol. Beijing*, 15(2008), No. 4, p. 389.
[9] S.K. Giri, T. Chanda, S. Chatterjee, and A. Kumar, Hot ductility of C–Mn and microalloyed steels evaluated for thin slab continuous casting process, *Mater. Sci. Technol.*, 30(2014), No. 3, p. 268.
[10] L. Yang, Y. Li, Z.L. Xue, and C.G. Cheng, Effect of different thermal schedules on ductility of microalloyed steel slabs during continuous casting, *Metals*, 9(2019), No. 1, art. No. 37.
[11] S. Ge, M. Isac, and R.I.L. Guthrie, Progress in strip casting technologies for steel; technical developments, *ISIJ Int.*, 53(2013), No. 5, p. 729.
[12] N. Zapuskalov, Comparison of continuous strip casting with conventional technology, *ISIJ Int.*, 43(2003), No. 8, p. 1115.
[13] Y. Kwon, J.H. Hwang, H.C. Choi, *et al.*, Microstructure and tensile properties of ferritic lightweight steel produced by twin-roll casting, *Met. Mater. Int.*, 26(2020), No. 1, p. 75.
[14] M. Ferry, *Direct Strip Casting Of Metals And Alloys*, Woodhead Publishing Limited, Cambridge, 2006.
[15] S. Ge, M. Isac, and R.I.L. Guthrie, Progress of strip casting technology for steel; Historical developments, *ISIJ Int.*, 52(2012), No. 12, p. 2109.
[16] Z.P. Xiong, A.G. Kostryzhev, N.E. Stanford, and E.V. Pereloma, Microstructures and mechanical properties of dual phase steel produced by laboratory simulated strip casting, *Mater. Des.*, 88(2015), p. 537.
[17] Z.P. Xiong, A.G. Kostryzhev, N.E. Stanford, and E.V. Pereloma, Effect of deformation on microstructure and mechanical properties of dual phase steel produced via strip casting simulation, *Mater. Sci. Eng. A*, 651(2016), p. 291.
[18] J.Y. Park, K.H. Oh, and H.Y. Ra, The effects of superheating on texture and microstructure of Fe–4.5wt%Si steel strip by twin-roll strip casting, *ISIJ Int.*, 41(2001), No. 1, p. 70.
[19] M.F. Lan, Y.X. Zhang, F. Fang, *et al.*, Effect of annealing after strip casting on microstructure, precipitates and texture in non-oriented silicon steel produced by twin-roll strip casting, *Mater. Charact.*, 142(2018), p. 531.
[20] Z.Y. Liu, Z.S. Lin, S.H. Wang, Y.Q. Qiu, X.H. Liu, and G.D. Wang, Microstructure characterization of austenitic Fe–25Mn–22Cr–2Si–0.7N alloy processed by twin roll strip casting, *Mater. Charact.*, 58(2007), No. 10, p. 974.
[21] M. Daamen, C. Haase, J. Dierdorf, D.A. Molodov, and G. Hirt, Twin-roll strip casting: A competitive alternative for the production of high-manganese steels with advanced mechanical properties, *Mater. Sci. Eng. A*, 627(2015), p. 72.
[22] C.J. Song, W. Lu, K. Xie, *et al.*, Microstructure and mechanical properties of sub-rapidly solidified Fe–18 wt%Mn–C alloy strip, *Mater. Sci. Eng. A*, 610(2014), p. 145.
[23] N. Yamauchi, A. Okamoto, H. Tukahara, *et al.*, Friction and wear of DLC films on 304 austenitic stainless steel in corrosive solutions, *Surf. Coat. Technol.*, 174-175(2003), p. 465.
[24] K. Mukunthan, P.D. Hodgson, P. Sellamuthu, L. Strezov, Y. Durandet, and N. Stanford, Castability and microstructural development of iron-based alloys under conditions pertinent to strip casting–specialty Fe–Cr–Al alloys, *ISIJ Int.*, 53(2013), No. 10, p. 1803.
[25] L. Liu, B.B. He, G.J. Cheng, H.W. Yen, and M.X. Huang, Optimum properties of quenching and partitioning steels achieved by balancing fraction and stability of retained austenite, *Scripta Mater.*, 150(2018), p. 1.
[26] P.S. Lyu, W.L. Wang, C.H. Wang, L.J. Zhou, Y. Fang, and J.C. Wu, Effect of sub-rapid solidification and secondary cooling on microstructure and properties of strip cast low-carbon bainitic–martensitic steel, *Metall. Mater. Trans. A*, 52(2021), No. 9, p. 3945.
[27] H. Xu, W.L. Wang, C. Lu, P.S. Lv, and C.Y. Zhu, Evolution of solidification structure for Si–Mn bearing AHSS under typical cooling rates, *J. Mater. Res. Technol.*, 15(2021), p. 524.
[28] R. Ranjan, H. Beladi, S.B. Singh, and P.D. Hodgson, Thermomechanical processing of TRIP-aided steels, *Metall. Mater. Trans. A*, 46(2015), No. 7, p. 3232.
[29] J. Speer, D.K. Matlock, B.C. De Cooman, and J.G. Schroth, Carbon partitioning into austenite after martensite transformation, *Acta Mater.*, 51(2003), No. 9, p. 2611.
[30] S.Z. Yin, A. Howells, D.J. Lloyd, M. Gallerneault, and V. Fallah, Thin strip vs direct chill casting: The effects of casting cooling rate on the As-cast microstructure of AA6005 Al–Si–Mg alloy, *Metall. Mater. Trans. A*, 53(2022), No. 6, p. 1928.